Available online at www.sciencedirect.com
SCIENCE DIRECT®
Geochimica et Cosmochimica Acta 70 (2006) 742–756
Geochimica
www.elsevier.com/locate/gca

Oxygen fugacity dependence of Os solubility in haplobasaltic melt

S.S. Fortenfant [a], D.B. Dingwell [b,*], W. Ertel-Ingrisch [b,c], F. Capmas [d], J.L. Birck [d], C. Dalpé [e,1]

[a] Bayerisches Geoinstitut, University of Bayreuth, D-95440 Bayreuth, Germany
[b] Earth and Environmental Sciences, University of Munich, Theresienstr. 41/III, D-80333 Munich, Germany
[c] Technical University of Ilmenau, Gustav-Kirchhoffstr. 1, D-98693 Ilmenau, Germany
[d] Laboratoire de Geochimie and Cosmochimie (UMR 7579 CNRS), Institut de Physique du Globe de Paris, Université Denis Diderot Paris 7, 4 place Jussieu, 75252 Paris Cedex 05, France
[e] Department of Earth Sciences, University of Bristol, Bristol BS8 1RJ, UK

Received 6 July 2004; accepted in revised form 3 October 2005

Abstract

Os equilibrium solubilities were determined at 1350 °C over a wide range of oxygen fugacities ($-12 < \log fO_2 < -7$) applying the mechanically assisted equilibration technique (MAE) at 10^5 Pa (= 1 bar). Os concentrations in the glass samples were analysed using ID-NTIMS. Additional LA-ICP-MS and SEM analyses were performed to detect, visualize and analyse the nature and chemistry of "nanonuggets." Os solubilities determined range at a constant temperature of 1350 °C from 0.63 ± 0.04 to 37.4 ± 1.16 ppb depending on oxygen fugacity. At the highest oxygen fugacities, Os^{3+} can be confirmed as the main oxidation state of Os. At low oxygen fugacities (below $\log fO_2 = -8$), samples are contaminated by nanonuggets which, despite the MAE technique, were still not removed entirely from the melt. However, the present results indicate that applying MAE technology does reduce the amount of nanonuggets present significantly, resulting in the lowest Os solubility results reported to date under these experimental conditions, and extending the experimentally accessible range of fO_2 for these studies to lower values. Calculated metal/silicate melt partition coefficients are therefore higher compared to previous studies, making Os more siderophile. Neglecting the as yet unknown temperature dependence of the Os metal/silicate melt partition coefficient, extrapolation of the obtained Os solubilities to conditions for core-mantle equilibrium, results in a $D_{Os}^{Fe\ liq,\infty/sil} = 1.5 \times 10^5$, while metallic alloy/silicate melt partition coefficients range from 1.4×10^6 to 8.6×10^7, in agreement with earlier findings. Therefore $D_{Os}^{met/sil}$ remains too high by 2–4 orders of magnitude to explain the Os abundance in the Earth's mantle as result of core-mantle equilibrium during core formation.

1. Introduction

Despite the development of increasingly sophisticated experimental and analytical methods in the last decade, accretion and core formation in Earth and other terrestrial planets is still a controversial subject in modern geochemistry. A debate remains between those supporting the fundamental idea of homogeneous accretion and core formation (e.g., Walter and Thibault, 1995; Li and Agee, 1996; Righter and Drake, 1997; Righter et al., 1997; Gessmann and Rubie, 1998, 2000; Li and Agee, 2001; Chabot and Agee, 2001, 2002), and others promoting the heterogeneous accretion and core formation idea (e.g., Wänke, 1981; O'Neill, 1991a,b; Ertel et al., 2001; Holzheid and Grove, 2002) including a final stage which is generally addressed as the "late veneer." One general point of agreement in the meantime is the presence of at least one, likely several, deep terrestrial giant magma ocean reservoirs over a wide range of pressure (20–60 GPa, corresponding to depths of 1200–1450 km), temperature (as high as 4000 K), and oxygen fugacity conditions (fO_2 from IW-0.5 to IW-2.4: Walter and Thibault, 1995; Li and Agee, 1996; Righter et al., 1997; Righter and Drake, 1997;

* Corresponding author. Fax: +49 89 2180 4176.
E-mail address: dingwell@lmu.de (D.B. Dingwell).
[1] Present address: Royal Canadian Mounted Police, P.O. Box 8885, 1200 Vanier Parkway, Ottawa, Ont., Canada K1G 3M8.

0016-7037/$ - see front matter © 2005 Elsevier Inc. All rights reserved.
doi:10.1016/j.gca.2005.10.004

Gessmann and Rubie, 1998, 2000; Li and Agee, 1996, 2001; Chabot and Agee, 2001, 2002). A representative overview is given in Walter et al. (2000).

Many discussions about accretion and core forming processes centre around the so-called "siderophile elements," and in particular, the highly siderophile elements (HSE), which consist of Pt, Rh, Ru, Os, Pd, Ir, and, based on their similar high metal/silicate melt partition coefficients ($D^{met/sil} \gg 10^4$) and depletions in the Earth (around 1000), Re and Au. Their geochemical behaviour makes them ideal indicators of core forming events, and their present distribution between core and mantle should contain information on the pressure, temperature and oxygen fugacity conditions, as well as phase compositions present during core formation (provided equilibrium was closely approached in those processes).

Two striking features of the highly siderophile elements have remained enigmatic for decades. First, their overabundances with respect to their large metal/silicate melt partition coefficients at 10^5 Pa (= 1 bar), which should have stripped them entirely into a newly formed metallic core, leaving no measurable trace of them back in the residual mantle. Second, their relative chondritic element ratios in Earth's upper mantle. The latter is especially surprising considering their vastly different geochemical behaviour at ambient pressures. These features of upper mantle HSE abundance patterns must be addressed by any model for accretion and core formation in the Earth.

Early partitioning experiments performed using the loop technique (Borisov et al., 1994; Borisov and Palme, 1995, 1996, 1997) exhibited a consequence of the experimental geochemistry of HSE which was unknown up to that time: the formation of nanonuggets of HSE, and resultant analytical challenges. Those authors speculated on either a lack of equilibrium between the metal loop and the silicate melt, or the presence of metal particles, (at that time called micronuggets) resulting in contamination of the analysed glasses and leading to erroneously high HSE solubilities using bulk analytical methods.

To improve the experimental results for siderophile elements in general, Dingwell et al. (1994) developed the mechanically assisted equilibration technique (MAE technique). This method is derived from a standard technique applied for melt homogenization in material and glass science. The basic idea involves the stirring out of nanonuggets by forced convection. The attainment of equilibrium under experimental conditions was also accelerated thereby. Obtained sample masses up to 1 g of glass enabled parallel analysis by several analytical techniques, both bulk (e.g., Instrumental Neutron Activation Analysis: INAA) and spot-analytical (Laser Ablation-Inductively Coupled Plasma-Mass Spectrometry: LA-ICP-MS) techniques, resulting in the first proof of the presence of nanonuggets in obtained LA-ICP-MS spectra (Ertel et al., 1999, 2001). Performing time-series sampling, the actual attainment of equilibrium can explicitly be demonstrated for each single experimental condition resulting in very reliable, high-quality, but time-consuming experiments. Ertel et al. (2001) demonstrated the presence of nanonuggets in Re-containing glass samples, and that steady state or homogeneity of analyses is not sufficient proof of equilibrium as is often inferred for the loop technique.

In such continuous studies, the mechanically assisted equilibration technique, in combination with LA-ICP-MS as a micro-analytical tool has greatly reduced the nanonugget influence in partitioning experiments concerning Pt, Rh (Ertel et al., 1999; Fortenfant et al., 2002), and Re (Ertel et al., 2001).

Borisov and Palme (1998) and Borisov and Walker (2000) reported first results on the effect of oxygen fugacity on the solubility of Os in silicate melt applying the loop technique. Their results showed substantial scatter in the data below an oxygen fugacity of $\log fO_2 = -8$, with no dependence on fO_2 below this value. This implies either zero valency, or a substantial nanonugget contamination problem. Given the successful results obtained for Pt, Rh and Re in 1 bar solubility studies using the MAE technique, we decided to reinvestigate the effect of oxygen fugacity on the solubility of Os in silicate melt as an attempt to improve the existing data, especially those obtained at low oxygen fugacity in the range $-12 < \log fO_2 < -7$.

2. Experimental method

A thorough description of the MAE technique itself and all experimentally necessary components as well as their specifications is given elsewhere (Dingwell et al., 1994; Ertel et al., 1996, 1997, 1999, 2001; Fortenfant et al., 2002), and all experiments here were performed according to those methods.

Briefly, the MAE technique requires a crucible and spindle made of the metal of interest. Os metal, however, is available commercially only as powder or in the form of Os alloys (e.g., iridosmium) which are known to be very brittle. A crucible and spindle made of pure Os was, based on its very high melting point (3593 °C) and its toxicity (Os may form toxic OsO_4) during melting, commercially not available, and was thus synthesized following Borisov and Palme (1998).

For this purpose, a mixture of 95 wt% Ni and 5 wt% Os was fused under very reducing conditions at 1650 °C for about 30 min. This liquid alloy was used to pour both a cylindrical crucible and a spindle head using Al_2O_3 moulds. In this way, a crucible of 30 mm height, 25 mm diameter and 2 mm wall thickness, which could hold approximately 30 g of silicate melt was manufactured. The head of the spindle made was 10 mm in length and 5 mm in diameter. This head was arc welded (under Ar) to a high purity (99.95%) Ni rod of 150 mm length and 5 mm diameter. During the experiment, care was taken to ensure that only the head of the spindle was in contact with the silicate melt.

Prior to any use in experiments, crucible and spindle compositions were determined using electron microprobe

(EMP) techniques as described below to check both the Ni–Os major element composition and homogeneity of crucible and spindle by analyzing pieces of crucible and spindle. Back scattered electron (BSE) images of the metal pieces revealed a quench-texture composed of two different phases. The two phases have been independently analysed by EMP using a 5 μm point beam. The bulk compositions of the Ni–Os alloy in crucible and spindle are given in Table 1. At run temperatures (1350 °C), however, the metal is believed to rehomogenize to a single, homogeneous phase.

A standard experiment consisted of loading the crucible with approximately 30 g of prefused and homogenized glass chips of AnDi eutectic composition, placing it in the hot zone of a vertical high temperature muffle tube furnace under controlled conditions of oxygen fugacity (e.g., for NiOs1 initial condition: $\log fO_2 = -12$, controlled by $CO–CO_2$ gas mixtures). Temperature was then raised to run temperature (1350 °C) and kept constant within ±1 °C. Once the glass chips were completely molten, the spindle was lowered into the melt and stirring was initiated. Sampling was performed once a week. For safety reasons and as protection against OsO_4-containing fumes, sampling of the experiment was performed wearing a gas mask equipped with a corresponding filter (A3 type) and safety glasses. As mentioned before, Os forms highly toxic OsO_4 if oxygen would accidently enter the furnace during sampling. After 5 weeks at $\log fO_2 = -12$, the oxygen fugacity was increased in steps of 1 log-unit every 5 weeks.

At the beginning of NiOs1, oxygen fugacity was constrained by pure CO_2 gas flowing through the muffle tube of the furnace. Oxygen fugacity was permanently monitored by an oxygen sensor directly placed below the crucible inside the hot spot of the muffle furnace. The emf (in mV) of the oxygen sensor was measured using a high-precision voltmeter and recorded on a chart recorder. This allowed us to reproducibly control and monitor our experiments over extended periods of time. To protect the entire laboratory against contamination with OsO_4, a monitoring system was connected to the voltmeter, interrupting the heating program if the emf decreased by more than 50 mV (corresponding to an increase of 0.06 log-units in fO_2). No such incident was observed during the entire performed experiments.

Table 1
Chemical composition of the Ni–Os alloy of spindle and crucible

	Ni (wt%)	SD	Os (wt%)	SD
Crucible				
Phase 1	92.4	1.3	7.6	1.1
Phase 2	96.9	0.5	3.1	1.4
Average	94.6	1	5.4	0.8
Spindle				
Phase 1	93.4	0.6	6.6	0.7
Phase 2	97.4	1.5	2.6	0.6
Average	95.4	1.2	4.6	0.7

Elemental concentration determined by EMPA using a point beam of 5 μm diameter, a beam current of 15 nA, an acceleration voltage of 15 keV, and 20 s of counting time for both elements. Pure Ni and Os metals were used as standards.

The starting material in all performed experiments corresponded to the 10^5 Pa (= 1 bar) Anorthite-Diopside (AnDi) eutectic composition, synthesized from pA grade SiO_2, $MgCO_3$, $CaCO_3$ and Al_2O_3 powders. Starting oxide components were intimately mixed together and subsequently fused in alumina crucibles in a high temperature Naber® box furnace at 1450 °C for about 45 min in air. The glass melt was quenched by removing the Al_2O_3 crucible from the furnace. The quenched glass was mechanically separated from the Al_2O_3 crucible, stored in a desiccator under vacuum, and used as starting material in all subsequent experiments after major element compositions had been verified by EMP analysis.

In experiments NiOs1 and NiOs2, initial Os concentrations were quite high, and equilibration periods, in consequence, were quite extensive. To avoid this problem likely due to a high oxygen concentration in the starting material during the initial phase of the experiments, AnDi starting material was produced under reducing conditions (1450 °C, $\log fO_2 = -10$) to avoid oxygen exposure of spindle and crucible, as a result high Os concentrations at the beginning of each subsequent experiment.

3. Analytical techniques

EMP analyses were performed at the Bayerisches Geoinstitut (University of Bayreuth, Germany) using a CAMECA SX-50 electron microprobe equipped with four wavelength-dispersive spectrometers applying a Pouchou and Pichoir (1984) correction procedure. The major alloy composition of the NiOs crucible and spindle was determined prior to any use by EMP analysis, using 15 nA current on brass, 15 keV acceleration voltage, 20 s counting time and a defocussed beam.

Major element (Si, Mg, Ca and Al) and Ni concentrations in the glass samples were determined on a routine basis. Each analysis consisted of three measurements (which were averaged) using an accelerating voltage of 20 kV, a beam current of 30 nA for major elements and 50 nA for Ni, and a counting time of 20 s for major elements and 100 s for Ni, respectively. Standards used were orthoclase (Si), enstatite (Mg), wollastonite (Ca), $MgAl_2O_4$ spinel (Al) and pure Ni. Major element concentrations of starting materials are averages of line profiles consisting of 20 points each. The chemical compositions of all starting glass materials used in the experiments are given in Table 2 as determined by EMP.

Os concentrations were determined at the Institute de Physique du Globe de Paris (IPGP, Paris) using Isotope Dilution-Negative Thermal Ion Mass Spectrometry (ID-NTIMS). The procedure used to perform the analyses is similar to Birck et al. (1997). ID-NTIMS measurements were carried out using a FINNIGAN MAT 262 mass spectrometer equipped with an electron multiplier with negative ion capability.

Table 2
Starting material compositions for each experimental run (in wt %)

Experiment	SiO_2[a]	Al_2O_3[a]	CaO[a]	MgO[a]
NiOs1	53.7	15.0	21.6	9.7
NiOs2	54.2	14.3	21.6	9.8
NiOs3	53.0	14.2	21.9	10.8
NiOs4	55.2	14.2	21.4	9.2

[a] EMP analyses were performed using 20 keV acceleration voltage, 50 nA current on brass, and 20 s counting time for each element. Standards used were orthoclase (Si), $MgAl_2O_4$ spinel (Al), wollastonite (Ca), enstatite (Mg). The precision of the measurement is ~0.4%.

At the beginning of the analytical procedure, Os is separated from the matrix by wet chemical treatment. The final Os separate is evaporated to dryness as $Os(Br)_6^{2-}$. The residue is dissolved in 1 μl of HBr and loaded on a Pt filament under a binocular microscope. Prior to the load the Pt is preheated to 1200 °C in air to ensure clean surfaces. The load is then covered with a mixture of $Ba(OH)_2$ and NaOH. The filament is quickly heated in air until the sample starts to melt and immediately afterwards quenched to a white layer. It is then inserted into the mass spectrometer in which an adjustable leak of water vapor saturated O_2 maintains a pressure of 2×10^{-7} torr in the source compartment. During slow heating to 800–850 °C, Os is emitted as OsO_3^- with yields of 3–20%. Only minor amounts of OsO_4^-, typically less than 1% of OsO_3^-, are released. When more than 0.5 ng have been separated, measurements are performed in the static multiple collector mode. The electron multiplier is run in the pulse counting mode resulting in an analytical precision in the range of 0.1% whereas the latter reaches 0.01% in the Faraday cup mode.

After correction of the contribution from the oxygen isotope ratios, Os concentrations are obtained from standard isotope dilution calculations. Standard solutions for Os were prepared from $(NH_4)_2OsBr_6$, a stoichiometric substance, thermally stable up to at least 120 °C (in air).

As mentioned earlier, LA-ICP-MS as a spot analytical tool, results, at present, in the most reliable results of partitioning experiments concerning HSE, based on its ability to avoid or minimize the nanonugget influence during the determination of elemental concentrations. Thus, LA-ICP-MS analyses were attempted at the University of Bristol (UK). The LA-ICP-MS system consisted of a LUV266X laser (New Wave Research, USA) linked to a PlasmaQuad3 with a supplement rotary pump attached to its interface (Thermo Elemental, UK). Unfortunately, existing standards for Os are based on NiS, which exhibit already a very high Os background. Accurate determinations of sub-ppm Os concentrations were therefore extremely difficult, and finally proved to be below detection limits. However, the presence of nanonuggets was able to be detected even though quantitative results were not obtainable (see Fig. 4). Until the advent of more advanced Os standards with a lower Os background, reliable Os determinations at sub-ppm levels cannot be obtained using LA-ICP-MS.

To check the presence, nature and chemical composition of nanonuggets in our glass samples, a Scanning Electron Microscopy study (SEM) was initiated. The SEM apparatus used for this study performed at the Bayerisches Geoinstitut (BGI, University of Bayreuth) was a Field Emission Gun Scanning Electron Microscope (FEG SEM) equipped with both Back Scattered Electron (BSE) detector and EDX system. Measuring conditions were 30 kV accelerating voltage and a magnification of up to 150×. Since Ertel et al. (1999, 2001) reported that nanonuggets are predominantly formed at extremely low fO_2 conditions, the Os-bearing glass samples obtained at $\log fO_2 = -12$ were investigated.

4. Results and discussion

At 1350 °C, nine experiments regarding the fO_2 dependence of Ni and Os over a wide range of fO_2 ($-12 < \log fO_2 < -7$) were performed using the MAE method of Dingwell et al. (1994), starting from the lowest fO_2 condition and increasing fO_2 during all subsequent experiments. The rationale behind this is that, as observed for other HSE (Ertel, 1996: Pt, Rh, Re and Ir), once having established equilibrium conditions, subsequent equilibrium solubilities are more easily obtainable in direction of higher than lower fO_2 conditions (Dingwell et al., 1994; Ertel, 1996). This strategy should help to speed up the total time of the entire study. All experimental conditions together with the raw ID-NTIMS analytical results are supplied in Table 3.

4.1. Equilibrium solubilities of Ni

Ni equilibrium solubilities can be obtained using the MAE technique of Dingwell et al. (1994) for equilibration times of ~400 h starting from a more reducing state and increasing oxygen fugacity, corresponding to oxidation of Ni. Since the equilibration period for Os was not known at the beginning of this study, equilibration periods of much more than 3 weeks (corresponding to 500 h or more) were assumed. Under such extensive equilibration periods, equilibrium solubilities for Ni were obtained under all experimental conditions investigated in this study. In consequence, Ni equilibrium solubilities were determined using steady state results obtained after more than 400 h of run duration—usually by using the last two analyses at the end of each fO_2 condition.

In general, Ni functions as an additional test element since experimental data on the partitioning of Ni between Ni metal and AnDi eutectic melt are already well established (Dingwell et al., 1994; Holzheid et al., 1994). Agreement between these data and the results of this study raises confidence in the quality of the present experimental partitioning data. For each fO_2, the new equilibrium concentration for Ni and Os in the melt was calculated by averaging the steady state values of Ni and Os at the end of each fO_2 step, representing the true equilibrium concentrations of Ni

Table 3
Experimental conditions of performed experiments

Sample[a] #	Time[b] [h]	emf[c] [mV]	$\log f O_2$[d] (sensor)	Ni[e] [ppm]	σ_{Ni}	Os[f] [ppb]	σ_{Os}
NiOs1 experiment (10^5 Pa, 1350 °C)—experimental conditions and results of EMPA and ID-NTIMS measurements							
0	0	908.1	−12.0	12	15	1.84	0.004
1	118	909.0	−12.0	177	18	9.98	0.020
2	262	910.0	−12.0	171	35	4.83	0.010
3	482	909.0	−12.0	180	29	4.67	0.009
4-1	604	909.1	−12.0	187	25	5.31	0.011
4-2	604	909.1	−12.0	187	25	5.31	0.011
4-3	604	907.4	−11.9	187	25	7.18	0.014
NiOs2 experiment (10^5 Pa, 1350 °C)—experimental conditions and results of EMPA and ID-NTIMS measurements							
0	0	904.5	−11.9	55	27	75.3	0.151
1	168	909.7	−12.0	169	28	78.5	0.157
2	332	911.5	−12.0	174	23	62.3	0.125
3	480	905.6	−11.9	176	21	49.3	0.098
4-1	619	911.0	−12.0	178	23	84.0	0.168
4-2	619	911.0	−12.0	178	23	19.1	0.038
5	789	911.4	−12.0	166	25	8.83	0.018
6	938	911.7	−12.0	165	28	9.55	0.019
NiOs3 experiment (10^5 Pa, 1350 °C)—experimental conditions and results of EMPA and ID-NTIMS measurements							
0	0	842.3	−11.1	20	23	96.5	0.193
1-1	215	838.5	−11.1	258	29	292.0	0.584
1-2	215	838.5	−11.1	258	29	487.0	0.973
2	477	836.5	−11.1	394	37	122.6	0.245
3	814	838.3	−11.1	418	25	38.6	0.077
4-1	933	829.2	−11.0	424	28	97.3	0.194
4-2	933	829.2	−11.0	424	28	36.3	0.073

Sample[a] #	Time[b]		emf[c] [mV]	$\log f O_2$[d] (sensor)	Ni[e] [ppm]	σ_{Ni}	Os[f] [ppb]	σ_{Os}
	Total	Rel.						
NiOs4 experiment (10^5 Pa, 1350 °C)—experimental conditions and results of EMPA and ID-NTIMS measurements								
0-1	0	0	800.0	−10.6	5	8	53.6	0.107
0-2	0	0	800.0	−10.6	5	8	11.31	0.023
1	210	210	839.5	−10.8	397	106	4.76	0.010
2-1	401	401	835.0	−11.0	396	33	23.49	0.047
2-2					396	33	10.38	0.021
3	551	551	841.0	−11.1	403	61	7.05	0.014
4-1	737	737	845.2	−11.2	400	33	21.60	0.043
4-2							19.44	0.039
4-3							32.77	0.066
5-1	883	883	846.5	−11.2	404	20	13.95	0.028
5-2							12.29	0.025
6-1	1052	1052	846.6	−11.2	398	21	70.75	0.142
6-2							62.9	0.126
6-3							27.74	0.055
7-1	1216	1216	846.7	−11.2	390	20	67.9	0.136
7-2							60.2	0.120
8	1388	1388	849.6	−11.2	405	29	79.3	0.159
9-1	1533	145	749.6	−10.0	1355	44	64.1	0.128
9-2							39.78	0.080
10-1	1648	260	741.3	−9.9	1487	272	53.1	0.106
10-2							24.83	0.050
11	2272	884	740.3	−9.9	1542	22	14.58	0.029
12	2272	884	737.4	−9.8	1538	43	43.20	0.086
13-1	2439	1051	750.5	−10.0	1584	37	9.46	0.019
13-2					1597	49	9.82	0.020
14	2612	1224	751.5	−10.0	1569	41	13.01	0.026
15-1	2775	1387	753.0	−10.0	1543	45	6.60	0.013
15-2							845.0	1.690
15-3							6.07	0.012
16-1	2943	168	683.5	−9.2	3938	591	7.90	0.016
16-2							23.75	0.048
17	3135	360	686.3	−9.2	4024	42	7.55	0.015

Table 3 (*continued*)

Sample[a] #	Time[b]		emf[c] [mV]	logfO_2[d] (sensor)	Ni[e] [ppm]	σ_{Ni}	Os[f] [ppb]	σ_{Os}
	Total	Rel.						
18-1	3303	528	684.1	−9.2	4056	59	3.82	0.008
18-2							3.51	0.007
19	3447	672	683.4	−9.2	4060	63	113.3	0.227
20-1	3620	845	684.5	−9.2	4078	38	5.97	0.012
20-2							4.23	0.008
21	3762	987	684.5	−9.2	4078	40	5.85	0.012
22	3980	218	604.5	−8.2	11094	1751	17.23	0.034
23	4144	382	604.3	−8.2	12067	262	1.09	0.002
24	4311	549	604.4	−8.2	11784	5406	0.91	0.002
25	4479	717	605.4	−8.2	11867	111	0.59	0.001
26	4649	887	604.0	−8.2	11929	226	0.67	0.001
27	4815	166	560.4	−7.6	19728	1835	0.64	0.001
28	4984	335	560.3	−7.6	21784	442	0.12	0.001
29	5175	526	559.6	−7.6	22196	201	2.52	0.005
30	5324	675	559.3	−7.6	22421	199	8.99	0.018
31-1	5415	766	560.3	−7.6	22289	188	1.87	0.004
32	5415	766	562.4	−7.7	22443	226	1.67	0.003
33	5603	954	560.2	−7.6	22131	176	1.71	0.003
34	5771	168	519.3	−7.1	37609	3838	1.02	0.002
35	5965	362	514.6	−7.1	33178	1320	3.17	0.006
36	6109	506	515.0	−7.1	38413	1306	6.18	0.012
37	6278	675	516.1	−7.1	40853	998	6.95	0.014
38	6445	842	512.7	−7.0	41615	358	0.95	0.002
39	6616	1013	514.4	−7.1	41435	207	2.14	0.004

Horizontal lines in Table 3 indicate termination of experiment or change of oxygen fugacity condition.
[a] Sample number.
[b] Time [tot] and Time [rel.] indicate absolute time in [hours] from start of experiment or relative time from last change of oxygen fugacity.
[c] emf in [mV] is voltage reading from voltmeter for measurement of oxygen fugacity.
[d] LogfO_2 recalculated from emf measurements.
[e] Ni concentration in glass sample in [ppm] as measured by EMP; SD as indicated.
[f] Os concentration in glass sample in [ppb] as measured by ID-NTIMS analyses; SD of measurement as indicated.

and Os. Obtained equilibrium values were then used to calculate the solubility of Ni and Os in 10^5 Pa (= 1 bar) AnDi eutectic melt at 1350 °C, using the following equation:

$$[M]_{eq} = \frac{[M]^{sil}_{exp}}{[M]^{met}_{exp} \times \gamma^{met}_{M}}, \quad (1)$$

where $[M]_{eq}$ is the equilibrium solubility of the element M dissolved inside the silicate melt starting from a pure crucible and spindle made of M, $[M]^{sil}_{exp}$ is the experimental concentration of the element M in silicate melt at equilibrium conditions dissolved from the alloy of crucible and spindle, $[M]^{met}_{exp}$ is the molar concentration of the element M in the alloy, and γ^{met}_{M} is the activity coefficient of M in the alloy.

The solubility of pure Ni in silicate melts was calculated assuming ideal behaviour of Ni in the Ni–Os alloy (i.e., $\gamma^{met}_{Ni} = 1$). This assumption was made based on two grounds: First, the Ni–Os alloy is very Ni-rich and consists mainly of Ni (98.4 mol% Ni), while Os is only 1.6 mol%. Second, Borisov and Walker (2000) demonstrated that the non-ideality of Ni in Ni–Os alloy is not very large. Taking this assumption as granted, calculated equilibrium data for Ni with $\gamma^{met}_{Ni} = 1$ for ideal behaviour are supplied in Table 4 for all runs performed at oxygen fugacities ranging from $-12 < \log fO_2 < -7$ (beside Os data assuming $\gamma^{met}_{Os} = 1$, and $\gamma^{met}_{Os} = 3.94$; compare discussion below). Obtained results for the equilibrium solubility of Ni in silicate melt (recalculated to $\gamma^{met}_{Ni} = 1$) in dependence of applied oxygen fugacity is graphically portrayed in Fig. 1, and compared to literature results (Dingwell et al., 1994; Holzheid et al., 1994; Borisov and Palme, 1998; Borisov and Walker, 2000).

Ni equilibrium solubilities plotted on a log solubility versus logfO_2 axis, increase linearly with increasing fO_2 values. Results of the present study are in excellent agreement with previously published results (Dingwell et al., 1994; Holzheid et al., 1994; Borisov and Palme, 1998; Borisov and Walker, 2000) as shown in Fig. 1. The slope through the data points plotted on a log solubility versus logfO_2 plot corresponds to the redox state of the corresponding element, and is 0.487 ± 0.008, corresponding to a valence state of 1.948 ± 0.032, and hence nearly undistinguishable to the ideal value of Ni^{2+} found in earlier studies. This slope is practically identical to 0.48 obtained by Borisov and Walker (2000) for experiments with Ni–Os alloy of comparable composition.

The excellent agreement between the Ni solubilities of the present study and those obtained in experiments with pure Ni as metallic phase confirms that the non-ideality of

Table 4
Equilibrium solubilities of pure Ni and Os in dependence of oxygen fugacity in AnDi 10^5 Pa eutectic melt composition at 10^5 Pa and 1350 °C

Run[a]	$\log fO_2$[b] (sensor)	Experimental data				Calculated solubilities assuming					
		Ni[c]		Os[d]		$\gamma_{Ni}^{met} = 1$[e]		$\gamma_{Os}^{met} = 1$[f]		$\gamma_{Os}^{met} = 3.94$[g]	
		[ppm]	SD	[ppb]	SD	[ppm]	SD	[ppb]	SD	[ppb]	SD
NiOs1	−12.0	185	3.03	5.6	0.94	188.5	3.08	325	53.4	82.4	13.5
NiOs2	−12.0	171	6.26	9.2	0.36	174.8	6.37	531	20.7	135	5.3
NiOs3	−11.0	422	2.83	37.4	1.16	429.4	2.88	2162	67	549	17.0
NiOs4	−11.2	398	5.50	13.1	0.83	404.6	5.60	758	48	192	12.2
NiOs4	−10.0	1,563	21.7	6.3	0.27	1,591	22.11	366	15.3	92.9	3.9
NiOs4	−9.2	4,074	7.8	5.3	0.79	4,145	7.93	309	45.9	78.4	15.3
NiOs4	−8.2	11,860	59.4	0.63	0.04	12,069	60.5	36.40	2.4	9.2	0.6
NiOs4	−7.6	22,321	125	1.75	0.09	22,714	127	101	5.1	25.6	1.3
NiOs4	−7.1	41,301	325	4.1	2.56	42,028	331	234	148	59.5	37.5

Calculations for Ni were performed assuming ideal behaviour of Ni in NiOs-alloy, so $\gamma_{Ni}^{met} = 1$. For Os, calculations were done for $\gamma_{Os}^{met} = 1$ (ideal behaviour of Os in the Ni–Os alloy), and $\gamma_{Os}^{met} = 3.94$ (assuming similar behaviour for Os as Re in Ni–Re alloy).

[a] Run number of experiment.
[b] Applied oxygen fugacity calculated from sensor emf.
[c] Ni concentration in glass sample determined from EMPA in [ppm]; SD from averaging process.
[d] Os concentration in glass samples determined by ID-NTIMS in [ppb]; SD from averaging process.
[e] Ni solubility recalculated according to ideal behaviour and SD from footnote c.
[f] Os solubility recalculated assuming ideal behaviour and std. deviation from footnote d.
[g] Os solubility recalculated assuming similar behaviour for Os as Re in Ni–Re alloy.

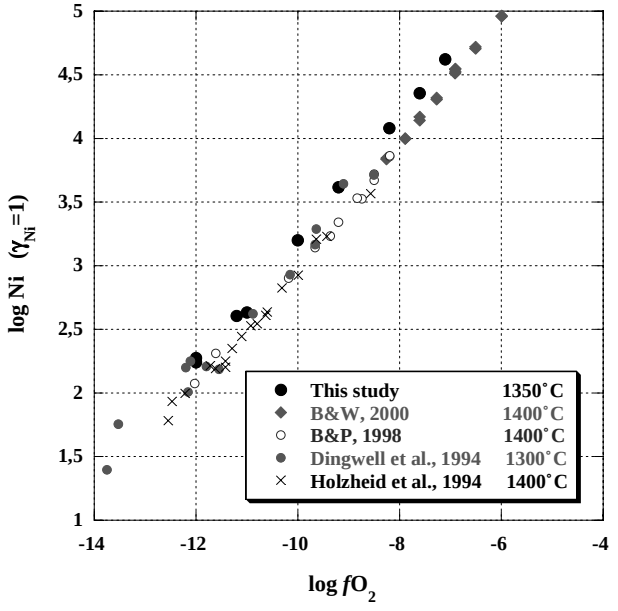

Fig. 1. Oxygen fugacity (fO_2) dependence of the Ni equilibrium solubility recalculated for $\gamma_{Ni}^{met} = 1$ in AnDi eutectic melt determined at 10^5 Pa. Plot of logarithm of Ni solubility (in ppm) versus $\log fO_2$. Error bars are smaller than the used symbol size. Previous data of Borisov and Walker (2000), Borisov and Palme (1998), Dingwell et al. (1994) and Holzheid et al. (1994) are given for comparison reasons. Corresponding experimental temperatures as indicated.

Ni in Ni–Os alloy is—as postulated by Borisov and Walker (2000)—not very large, and validates the assumption of ideal behaviour of Ni in Ni–Os alloy for calculation of Ni equilibrium solubilities and partition coefficients in the present study. This additionally lends credence to the performed experiments and their results, and it can be assumed that the solubility data for Os do reflect the true oxygen fugacity dependent equilibrium solubility values.

4.2. Equilibrium solubilities of Os

It is unfortunate in light of the Ni–Os alloy employed (~1.7 mol% Os), that thermodynamic data for the Ni–Os binary system are still lacking. Thus, recalculations of the experimentally determined solubilities of Os are not trivial. However, Borisov and Walker (2000) noticed that both Re and Os, having very high melting temperatures and the identical, hexagonal structure, should behave chemically similarly. Thus, the Ni–Os phase diagram should be very similar to that of Ni–Re. Using this assumption, thermodynamic data from Okamoto (1992) could be used to estimate the activity coefficient of Os in the Ni–Os alloy. From Okamoto (1992), the equation of the excess Gibbs energy of mixing of the face-centered-cubic (fcc) phase of Ni–Re alloy is:

$$\Delta_{mix}G^{ex}_{Ni-Re}(fcc) = X_{Re}(1 - X_{Re})(17750 + 41845X_{Re}), \quad (2)$$

where X_{Re} is the molar fraction of Re in the alloy. The Ni–Os alloy used in the present study contains 1.7 mol% of Os. For this Os content (X = 0.017), using Eq. (2), the activity coefficient for Os is calculated to be 3.94 at 1350 °C (see calculation procedure in Fortenfant et al., 2002). Based on this assumption, the activity of Os in the Ni–Os alloy may then lie between 0.017 (ideal behaviour) and 0.067 (assuming similar chemical behaviour of Ni–Re and Ni–Os alloy). Both values were used to recalculate the experimentally determined Os concentrations to solubilities of pure metallic Os in AnDi eutectic melt under experimental conditions as supplied in Table 3. Experimental conditions, obtained raw solubilities of Ni and Os as well as results of

the recalculation to pure Os metal conditions are shown in Table 4. Values of Os solubilities calculated for $\gamma_{Os}^{met} = 1$ and $\gamma_{Os}^{met} = 3.94$ differ by approximately 0.6 log-units. For further discussion, exclusively solubility values calculated for $\gamma_{Os}^{met} = 1$ will be considered, keeping in mind that these values represent only upper limits of the determined Os solubilities in respect to the nanonugget formation issue.

Results of raw Os solubilities as determined by ID-NTIMS are, for comparison reasons with Borisov and Palme (1998) and Borisov and Walker (2000), shown in Fig. 2. Recalculations to conditions of $\gamma_{Os}^{met} = 1$, and a corresponding literature comparison are graphically displayed in Fig. 3, while for more detailed discussion and comparison reasons, the fO_2 range $-5.5 < \log fO_2 < -8.5$ is enlarged in Fig. 4.

Os equilibrium solubilities were determined from raw ID-NTIMS results (as shown in Table 3) by using steady state results—usually the last two data points at maximum run duration. Usual equilibration durations for Os were originally assumed to be at least 500 h, while most data are obtained for run durations of 800–1000 h. In the case of the NiOs4 experiment ($\log fO_2 = -11.2$), equilibrium obtained after 883 h was considered final due to a most probable reoxidation event which increased the Os solubilities after this period of time (comp Table 3). Analyses displaying serious nanonugget contamination due to extraordinary high Os concentrations were excluded from the concentration determination process as well. Os solubilities, determined by ID-NTIMS, range from 0.63 ± 0.04

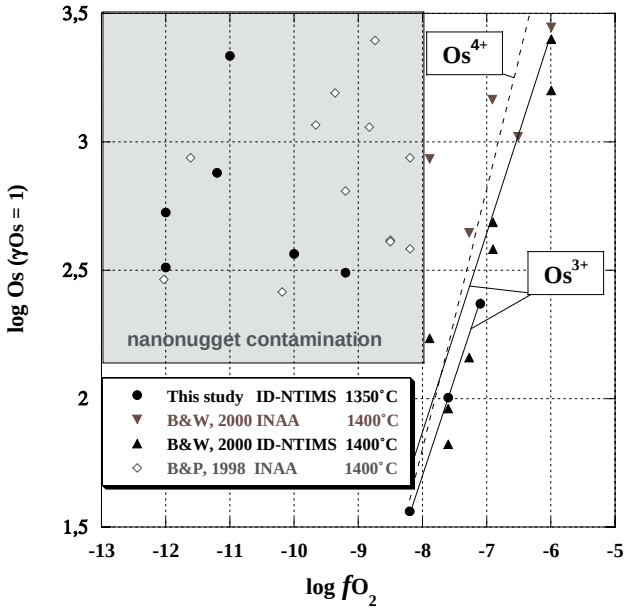

Fig. 3. Oxygen fugacity (fO_2) dependence of the solubility of Os in AnDi eutectic melt determined at 10^5 Pa over oxygen fugacity range investigated ($-12 < \log fO_2 < -7$). All data are recalculated assuming ideal behaviour for Os in Ni–Os alloy ($\gamma_{Os}^{met} = 1$). Data by Borisov and Walker (2000) and Borisov and Palme (1998) would be offset by ~0.6 log units in case of non-ideal behaviour of Os in Ni–Os alloy ($\gamma_{Os}^{met} = 3.94$ at 1350 °C, and $\gamma_{Os}^{met} = 4.2$ at 1400 °C). Range of increased nanonugget formation and increased contamination problem during ID-NTIMS analyses as indicated. Regression lines with slopes for Os^{3+} (solid line) and Os^{4+} (dashed line) as indicated.

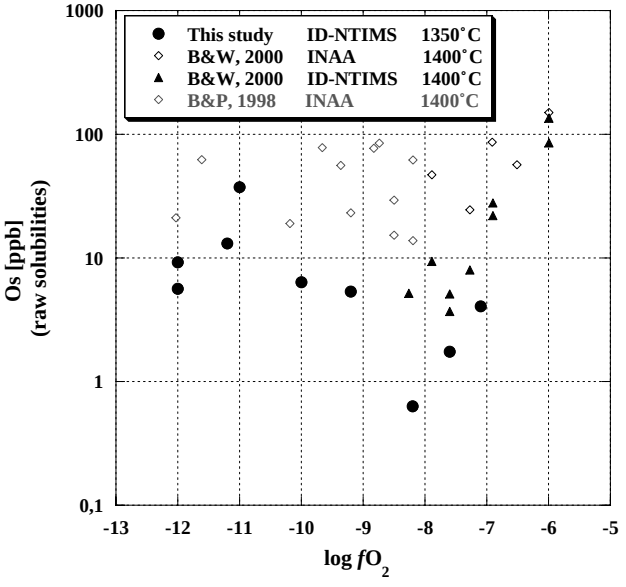

Fig. 2. Oxygen fugacity (fO_2) dependence of the solubility of Os in AnDi eutectic melt determined at 10^5 Pa over oxygen fugacity range investigated ($-12 < \log fO_2 < -7$). Os concentrations in glass samples as determined from ID-NTIMS measurements ("raw solubilities": uncorrected for alloy composition) are plotted versus $\log fO_2$. Uncorrected data from Borisov and Palme (1998); (INAA), and Borisov and Walker (2000): (both INAA and ID-NTIMS) are supplied for direct comparison reasons (see text for discussion).

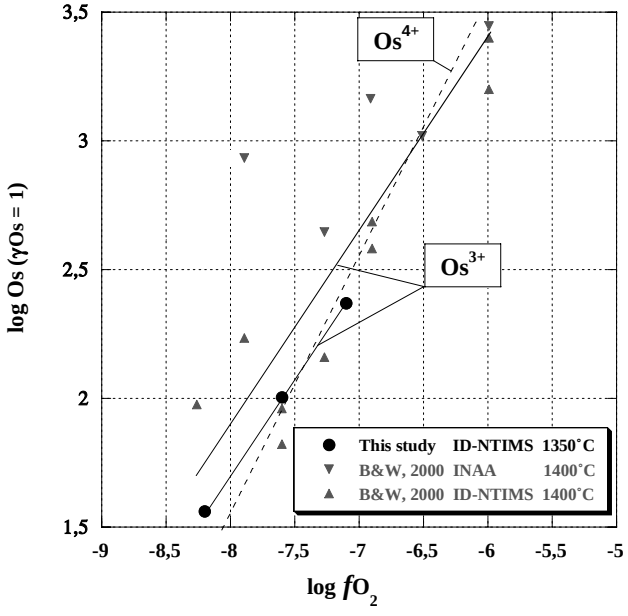

Fig. 4. Oxygen fugacity dependence of pure Os solubility in AnDi 10^5 Pa eutectic melt at high temperatures for oxygen fugacities between 10^{-5} and 10^{-9} bars outside the range of dominating nanonugget contamination. Comparison with Borisov and Walker (2000) INAA and ID-NTIMS data. Regression lines with slopes corresponding to Os^{3+} (solid line) and Os^{4+} (dashed line) as indicated.

up to 37.42 ± 1.16 ppb, corresponding to Os solubilities recalculated for pure Os as crucible and spindle material ($\gamma_{Os}^{met} = 1$) of 36.40 ± 2.37 to 2162 ± 67 ppb. Some analyses reveal Os concentrations of up to 25,000 ppb, showing clear evidence for excessive nanonugget contamination.

Fig. 2 shows a similar comparison of raw Os solubility results (not corrected for γ_{Os}^{met}) in respect to applied oxygen fugacity and indicated temperature as determined by ID-NTIMS from experiments in the literature and the present study—as already supplied in Borisov and Walker (2000). Remarkably, results of the present study do plot either on the lower limits of determined solubilities of previous literature investigations, or clearly below previously determined Os solubilities (e.g., at fO_2 conditions between $10^{-8.2}$ and $10^{-7.1}$ bars).

It should be noted that as metal solubilities depend on alloy composition as well as on temperature, the results of this kind of comparison are not unexpected as the Ni–Os alloys used consisted of varying amounts of Os. Borisov and Palme (1998) used Ni–Os alloys with Os mole fractions of 0.034–0.029, while Ni–Os alloys of Borisov and Walker (2000) contained 0.053–0.059 mol% Os. The Ni–Os alloy of the present study contained only 0.017 mol% Os, which is only a third to a half of Os concentrations previously used. Furthermore, Borisov and Palme (1998) and Borisov and Walker (2000) performed their loop experiments at 1400 °C in comparison to experiments of the present study using the MAE method, performed at 1350 °C.

It is therefore remarkable, that the Os solubility data do plot on the lower limits of previously determined investigations showing minimum nanonugget influence while a clear solubility trend (admittedly only constrained by three data points) can be obtained even further down to lower oxygen fugacities using identical analytical technologies (ID-NTIMS). This observation can only be explained by a reduction of the nanonugget effect due to the difference in applied experimental technology (MAE method versus loop technique), and its cleaning effect due to forced convection. This is an important observation with respect to HSE partitioning experiments since the nanonugget effect requires the most capable experimental technique to avoid or reduce nanonugget formation or contamination coupled with most advanced analytical techniques capable of avoiding nanonugget contamination influence during elemental concentration determinations.

Obtained solubility results for Os, as shown in Fig. 2, were recalculated to $\gamma_{Os}^{met} = 1$ and plotted together with literature results recalculated to identical conditions. Results are graphically portrayed in Fig. 3. For the present author, Fig. 3 is an impressive demonstration of the problems existing with HSE partitioning experiments using bulk analytical technologies. Starting from relatively high fO_2 conditions around $\log fO_2 = -7$, Os solubilities of the present study decrease with decreasing fO_2 as expected, assuming a dissolution mechanism based on oxidized species (Os^{n+}) in the melt. This systematic decrease with decreasing oxygen fugacity is both obvious in the present data set as well as in Borisov and Walker (2000). Below a threshold of around $\log fO_2 = -8.3$, no clear trend of elemental solubilities with further decreasing fO_2 is visible any longer, and the scatter of obtained data is significant allowing no interpretation of obtained data at all. An improvement of obtained data is visible in the Borisov and Walker (2000) study applying ID-NTIMS techniques with respect to the Borisov and Palme (1998) data using INAA techniques. With this improvement, Borisov and Walker (2000) were able to determine the oxidation state of Os in silicate melts as discussed below.

Fig. 4 gives a more detailed view of the fO_2 range between $-5.5 < \log fO_2 < -9$, indicating three data points obtained at relatively high fO_2 of the present study in comparison to results of Borisov and Walker (2000). It is necessary to point out that Borisov and Walker (2000) performed their experiments at 1400 °C while the present study was performed at a slightly lower temperature of 1350 °C. A slight offset of the two data sets are most probably due to the difference in absolute temperature. Unfortunately, only three data points of the present study seem to be unaffected by the nanonugget influence, and can be used to determine the oxidation state of Os inside the silicate melt. A fit through the obtained three data points of the present study results in a slope of 0.736 ($r^2 = 0.999$), corresponding to a valence state of Os of 2.94.

$$\log[Os]_{sil}(ppb) = 0.736 \cdot \log fO_2 + 7.594 \qquad (r^2 = 0.999). \qquad (3)$$

Based on this restricted data set, the main oxidation state of Os in the melt is determined to be Os^{3+}, while some influence of higher or lower oxidation states (Os^{4+}) cannot be detected or confirmed. This is in agreement with findings of Borisov and Walker (2000) proposing a main valence of Os of 3+ in the silicate melt, with only minor influence of Os^{4+}.

As already mentioned, below a threshold around $\log fO_2 \sim -8.3$, the observed trend of decreasing solubility with decreasing fO_2 disappears, equilibrium conditions become more difficult to be detected, data start to scatter significantly, and measured solubilities even seem to increase with decreasing fO_2 conditions (comp Fig. 2), if all data of the present study are taken into consideration performing a regression. This is, of course, absurd since this would imply a sudden change to an anionic dissolution mechanism for Os. However, identical observations at low fO_2 conditions were made by Ertel (1996) for Ir, Pt, Rh, and by Ertel et al. (2001) for Re, and Borisov and Palme (1997, 1998) and Borisov and Walker (2000), for Ir, Pt and Os if bulk analytical INAA techniques for concentration determinations were used. This observation is, therefore, qualitatively in complete agreement with previous studies.

As mentioned earlier, the original intension was to apply LA-ICP-MS in this study to detect and avoid nanonugget contamination in the measurements. However, since available standards for Os were fraught with difficulties surrounding high background and low signal intensities,

making LA-ICP-MS measurements on the observed Os concentration level impossible, ID-NTIMS analyses had to be performed in lack of a more appropriate spot analytical method. Nevertheless, the determination of Os equilibrium solubilities at low fO_2 conditions remains problematic, and gets even worse with further decreasing fO_2 conditions visible in some increase of the solubility trend. In consequence, data below $\log fO_2 < -8$ show a significant scatter over one order of magnitude, similar to observations made by Borisov and Palme (1998). Looking at the actual data in Table 3, results of time series do still level out. However, some results show suddenly orders of magnitude higher Os concentrations, while some show Os concentrations about 50% lower than the average value. This is clear indication for extensive nanonugget influence in the performed analyses. Cross checks using LA-ICP-MS technique detected clearly presence of nanonuggets without supplying any quantitative useful information. In this respect, the true Os equilibrium solubility stays hidden behind a contribution to the concentration based on nanonuggets distributed over the entire sample.

Based on these analytical results, it is clear that it is not possible to prove that the MAE method removes nanonuggets completely. However, even if the MAE technique cannot entirely remove all nanonuggets from the melt, it is, on the basis of these results, clearly the best method employed to date to reduce their presence. This is demonstrated by (1) the more coherent trend between solubility versus oxygen fugacity data, (2) less scatter in the measured absolute solubility values, (3) the extension of the observed linear solubility trend with $\log fO_2$ down to lower fO_2 values, and most importantly, (4) the extension of the data set to lower absolute Os solubility levels. All this is clearly demonstrated in Fig. 2. It should be noted in addition, that all existing high-quality LA-ICP-MS standards used for analyses of HSE on the trace element level, have been synthesized exclusively by the use of the above mentioned MAE technique. It is indispensable for these standards to be essentially nanonugget-free, with a constant and homogeneous HSE concentration on the ppb-level. Nevertheless, in the absence of reliable Os standards and more sophisticated microanalytical treatment of the present data, we cannot entirely exclude nanonuggets here and, as a result, the presented solubilities must be treated as upper limits. Correspondingly, and importantly, the determined Os metal/silicate melt partition coefficients remain lower limits.

4.3. Nanonugget investigations using LA-ICP-MS and SEM analyses

The presence of nanonuggets in glass samples from metal/silicate melt partitioning experiments is now commonly recognized (Borisov and Palme, 1997; Ertel et al., 1999, 2001). However, no visualization and/or identification has yet been provided. In an attempt to visualize the nanonuggets, LA-ICP-MS analyses of some samples, and an imaging study of some of the Os-bearing glass samples of the present study was performed using a LEO Gemini 1530 Field Emission Gun Scanning Electron Microscope (FEG SEM) of the Bayerisches Geoinstitut (University of Bayreuth) equipped both with BSE and EDX detector.

Fig. 5 shows results representative for the LA-ICP-MS analyses performed. The analytical procedure was identical

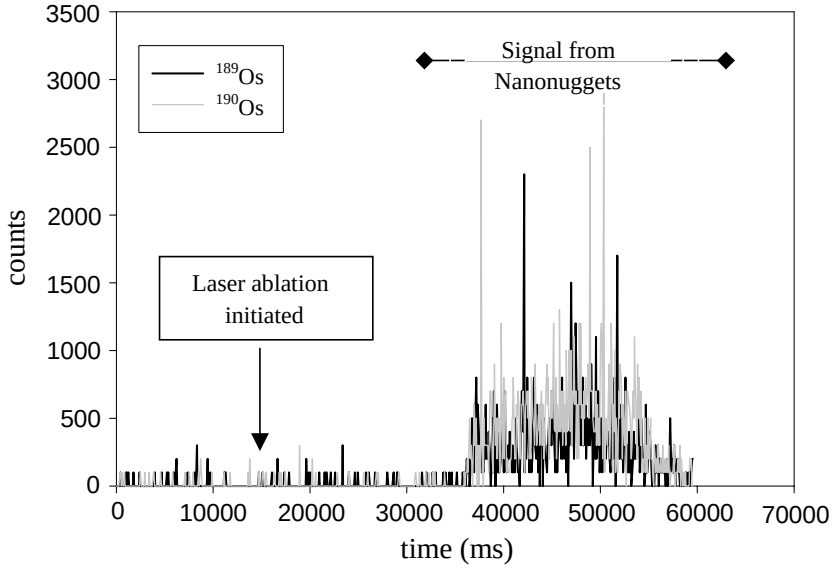

Fig. 5. LA-ICP-MS signal (in raw counts) versus ablation duration in ms. for the isotopes ^{189}Os and ^{190}Os from analysis of sample NiOs4–8. Os ablation and, in consequence, a LA-ICP-MS ablation signal is expected to appear when the laser ablation is started (“Laser Ablation initiated”) at 15 s after start of analysis. However, Os signal remains below detection limit. After 37 s, Os containing nanonuggets are hit and ablated by laser beam visible in a hill-like signal with overlying spikes—as indicated with “Signal from Nanonuggets”. Signal continues until 58 s, and decays afterwards. Os analysis by ID-NTIMS resulted in 79 ppb.

to those described by Ertel et al. (1999, 2001), and derived from procedures of Sylvester and Eggins (1997). After 15 s of collection of background signal, the laser was focused onto the sample (as indicated by "Laser ablation initiated" in Fig. 5), and the ablation spectrum was collected. As described in Ertel et al. (1999, 2001), hills and spikes in LA-ICP-MS spectra are direct experimental evidence for the presence of nanometer sized particles, or nanonuggets. The spectrum shows a smooth signal for 37 s after laser ignition. After 37 s, the ablation spectra shows suddenly a hill like structure with overlying spikes due to the ablation of an sample area highly contaminated with nanonuggets of various size and concentration. Signal intensities, effectively free of nanonuggets (like the signal up to 37 s after laser ignition) would, of course, result in up to two orders of magnitude smaller Os concentrations—even if the shown ablation spectrum is clearly below detection limit.

To additionally visualize and potentially determine the size and elemental composition of the nanonuggets detected by LA-ICP-MS, SEM analyses with an EDX detector were performed using magnifications of approximately 120× to 160×. In these analyses, bright, round spots of approximately 100–200 nm were found as shown in Fig. 6A, with a very scarce spatial distribution of 1–3 nanonuggets in a sample area of approximately 3 mm^2. The EDX detector determined reflections for the elements Si, Ca, Al, Mg and Ni, as indicated in Fig. 7B. Based on these determinations, a Ni/Si ratio of 0.07 was detected, which indicates a slightly enrichment in Ni in respect to the original ratio of 0.001 found in the starting glass sample as determined by electron microprobe. The nanometer sized "nanonuggets" detected here can, therefore, only be characterized as tiny, Ni-rich metallic particles. Whether these nanonuggets contain Os as well is still unclear since Os cannot be detected by EDX.

Ertel et al. (1999) estimated the average size of the particles to be approximately 0.05–0.2 μm. In consequence, they were called nanonuggets since their size is of nanome-

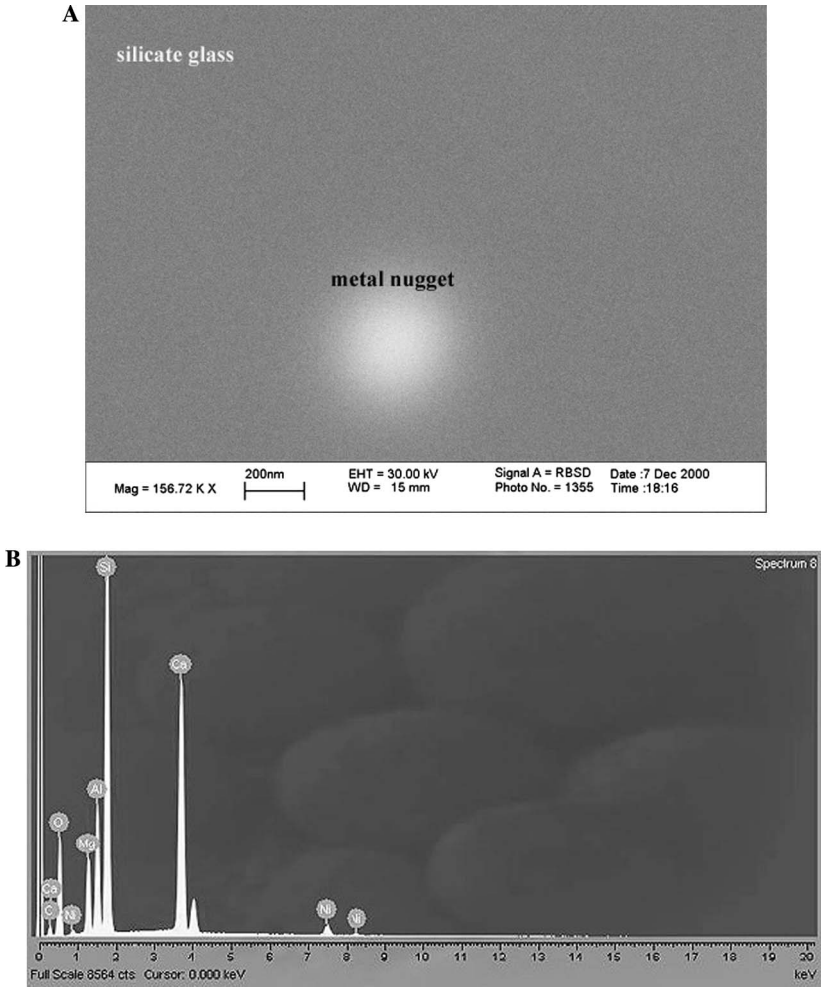

Fig. 6. SEM image of sample NiOs1–5 with the image of a detected nanonugget visible as bright, round spot in the lower part of image. A Ni-rich multi-element metallic nanonugget (comp Fig. 7B) of approximately 200 nm size is visible in the glass sample. (B) Corresponding EDX spectra of sample NiOs1-5 as shown in (A). Lines for Ca, Mg, Al, Si and Ni are indicated. The detection of these lines in the nanonugget indicate a multi-component composition of the elements mentioned. An origin as chipped off piece of crucible or spindle can be excluded since this would comprise only of Ni and Os which is, however, technically not detectable under an EDX detector.

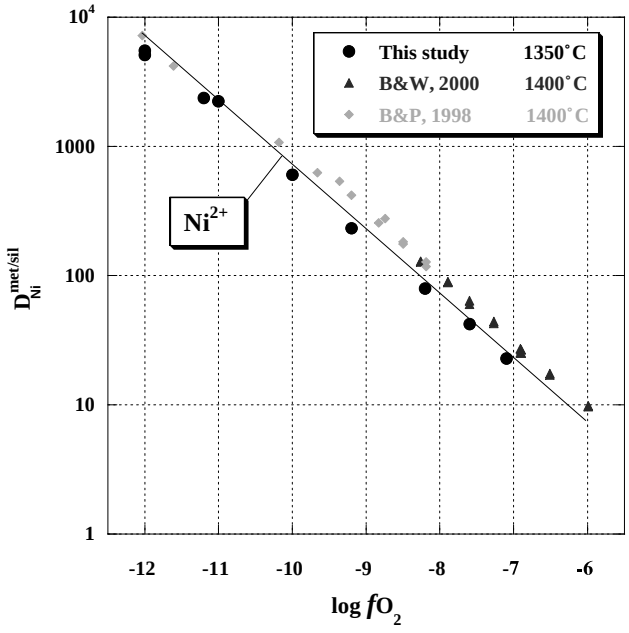

Fig. 7. Plot of $D_{Ni}^{met/sil}$ (calculated as weight ratio of Ni in NiOs alloy versus Ni concentration in silicate glass) in dependence of applied oxygen fugacity. For comparison with literature results, Borisov and Palme (1998) and Borisov and Walker (2000) data are shown. A regression line with a slope corresponding to pure Ni^{2+} (solid line) is supplied.

ter scale. Determined sizes of identified nanonuggets are in excellent agreement with those estimations. However, knowledge about their size does not include any information about their origin. The determined mixture of Si, Al, Ca, Mg and Ni (with or without traces of Os), however, makes an origin as chipped-off pieces of crucible or spindle unlikely since such pieces would mainly consist of Ni without detectable amounts of Si, Al, Ca and Mg as detected above. Results of the SEM analyses pinpoint in direction of an origin as result of an exsolution process most likely due to a change in oxygen fugacity, creating a kinetically and thermodynamically stable exsolution phase in the melt. Such phase would as well be hard to be stirred out of melts, if once formed, since reprecipitation on Ni surfaces (even if it is Ni–Os alloy) would be favoured for an identical phase and not a mixture of all kinds of melt components (or oxide phases). Dingwell et al. (1994) observed in Ni experiments, that Ni spindle and crucible aggregated upon contact. This mechanism would exclude any possibility for a Ni nanonugget existing for any longer period of time.

5. Implications for core formation models

For existing models for accretion of the Earth, including giant magma ocean scenarios during core formation (e.g., Li and Agee, 1996; Righter et al., 1997; Righter and Drake, 1997; Gessmann and Rubie, 1998, 2000; Li and Agee, 2001; Chabot and Agee, 2001, 2002), partition coefficients of the HSE between liquid metal and silicate melt at geochemically relevant conditions are required. One major variable is the oxygen fugacity dependence of the solubility, and as a result, the partition coefficient.

Metal/silicate melt partition coefficients for Ni were recalculated as simple weight ratio of the Ni concentration in the NiOs to the Ni concentration in the silicate glass (as supplied in Table 5), and graphically portrayed in Fig. 7. For comparison with previous studies, data from Borisov and Palme (1998) and Borisov and Walker (2000) are supplied together with a regression line for an oxidation state of Ni of 2+. Results of the present study are in excellent agreement with previous determinations of $D_{Ni}^{met/sil}$, and add additional credence to the quality and reliability of the obtained values of $D_{Os}^{met/sil}$.

Metal/silicate melt partition coefficients for Os can be estimated using the solubility-fO_2 equation that has been obtained in the present study for $\log fO_2 > -8$ (Eq. (3)). Conditions in the magma ocean were likely around 2500–3000 K, and an oxygen fugacity about 2 log-units below the iron-wüstite buffer (IW) corresponding to an absolute oxygen fugacity of $10^{-4.2}$ bars at 3000 K, calculated using the μ_{O2} −T equation for the Fe-FeO system from O'Neill and Pownceby (1993), and correcting for the melting of Fe using the thermodynamic data from Swartzendruber and Sundman (1983).

Using Eq. (3), the solubility of pure Os in the silicate liquid can be estimated to be 31.9 ppm at conditions relevant

Table 5
Ni and Os concentrations in silicate and alloy phase at 1350 °C, and corresponding metal/silicate partition coefficients for Ni and Os

Experiment	$\log fO_2$	Ni[a] (glass) [ppm]	Os[a] (glass) [ppb]	Ni[b](alloy) [wt%]	Os[b] (alloy) [wt%]	$D_{Ni}^{met/sil}$	$D_{Os}^{met/sil}$
NiOs1	−12.0	184.7	5.618	94.6	5.4	5122	9,612,000
NiOs2	−12.0	165.5	9.188	94.6	5.4	5716	5,877,000
NiOs3	−11.0	422.0	37.419	94.6	5.4	2242	1,443,000
NiOs4	−11.2	397.7	13.120	94.6	5.4	2379	4,116,000
NiOs4	−10.0	1573	6.339	94.6	5.4	601	8,519,000
NiOs4	−9.2	4078	5.347	94.6	5.4	232	10,099,000
NiOs4	−8.2	11898	0.630	94.6	5.4	80	85,714,000
NiOs4	−7.6	22288	1.749	94.6	5.4	42	30,875,000
NiOs4	−7.1	41525	4.055	94.6	5.4	23	13,317,000

[a] Ni and Os concentrations in the glass phase determined by EMPA and ID-NTIMS, respectively.
[b] Ni and Os concentration (in wt%) in the alloy phase determined by EMPA. $D_{Ni}^{met/sil}$ and $D_{Os}^{met/sil}$ calculated by dividing elemental concentrations in alloy and silicate glass phase.

for core formation ($\log fO_2 = -4.2$). Of course, the temperature dependence of Os solubility in silicate melt is to date still unknown, and therefore this value cannot be extrapolated to temperatures of 3000 K required for a deep magma ocean model. The partition coefficient of a metal element M between silicate melt and Fe-rich liquid, $D_M^{\text{Fe liq},\infty/\text{sil}}$, can be deduced from its solubility in melt, $[M]_{sil}$, at high temperature according to Eq. (4)

$$D_M^{\text{Fe liq},\infty/\text{sil}} = \frac{[M]_{met}}{[M]_{sil}} = \frac{1}{[M]_{sil} \times \gamma_M^{\text{Fe liq},\infty \times A}}, \quad (4)$$

where $\gamma_M^{\text{Fe liq},\infty}$ is the activity coefficient of M at infinite dilution in liquid Fe referred to a standard state of pure solid metal M at the conditions of the experiment, and A is the converting factor from molar fractions to weight fractions. At infinite dilution in liquid Fe, the converting factor A is equivalent to the ratio of the molar mass of Fe (55.8 g/mol) to the molar mass of the element M. For Os, A is then equal to 0.29. The activity coefficient of Os at infinite dilution in liquid metal is calculated as described in Fortenfant et al. (2002). Using the excess Gibbs energy of mixing for the binary Fe–Os system given in Swartzendruber and Sundman (1983), the following expressions can be used to calculate the activities of Os in liquid Fe referred to a standard state of pure solid Os at the conditions of the experiment

$$RT \ln \gamma_{Os}^{\text{Fe liq},\infty} = 16.782\text{–}0.00837\ \ T \quad (\text{in kJ/mol}). \quad (5)$$

At 3000 K, and infinite dilution in liquid Fe ($X_{Os} \to 0$), $\gamma_{Os}^{\text{Fe liq},\infty}$ calculated using Eq. (5) is 0.716. Using the estimated values of $\gamma_{Os}^{\text{Fe liq},\infty}$ and the extrapolated solubility value for Os of 31.9 ppm at an oxygen fugacity 2 log units below IW, the liquid Fe/silicate melt partition coefficients for Os calculated using Eq. (4) is $D_{Os}^{\text{Fe liq},\infty/\text{sil}} = 1.5 \times 10^5$. However, it has to be mentioned that in our estimation of $D_{Os}^{\text{Fe liq},\infty/\text{sil}}$, the dependence on temperature (even though that $\gamma_{Os}^{\text{Fe liq},\infty}$ was estimated for 3000 K), pressure, silicate or sulfide melt composition has not been taken into account.

Borisov and Palme (1998) estimated their metal/silicate melt partition coefficients for Os by dividing the amount of Os in the alloy by the amount of Os in the silicate glass, resulting in $D_{Os}^{met/sil}$ between 1.2×10^6 to 1.1×10^7. Similar treatment of the Borisov and Walker (2000) data result in values ranging from 1.0×10^6 to 4.3×10^7. Identical recalculations of the present study result in $D_{Os}^{met/sil}$ ranging from 1.4×10^6 to 8.6×10^7, and are, therefore, in good agreement with previous findings. Results of these recalculations for the present study are supplied in Table 5 and shown in Fig. 8 together with an identical treatment of the Borisov and Palme (1998) and Borisov and Walker (2000) data. Regression lines representing either pure Os^{3+} or pure Os^{4+} are additionally supplied. Remarkable is the good agreement with the Borisov and Walker (2000) data using identical analytical techniques for the determination of the Os concentration (ID-NTIMS), while the present three data points are situated on the upper limits of the data set determined by Borisov and Walker (2000).

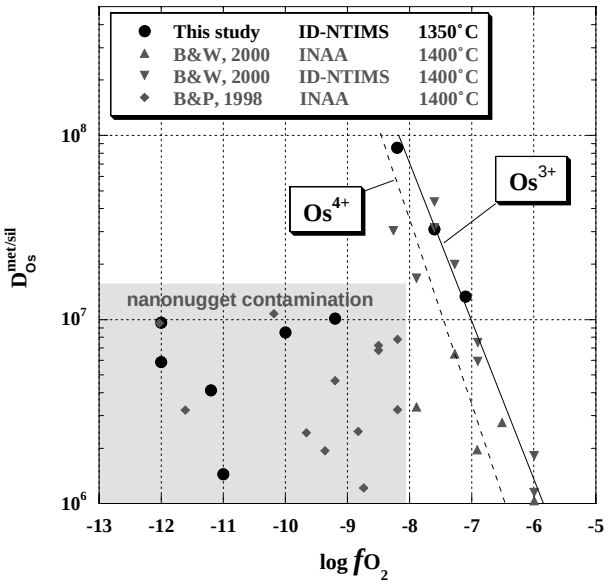

Fig. 8. Plot of $D_{Os}^{met/sil}$ (calculated as weight ratio of Os in NiOs alloy versus Os concentration in silicate glass) in dependence of applied oxygen fugacity. For comparison with literature results, Borisov and Palme (1998) and Borisov and Walker (2000) data are shown. Regression lines with slopes corresponding to Os^{3+} (solid line) and Os^{4+} (dashed line) are supplied.

Starting from the highest fO_2 conditions, $D_{Os}^{met/sil}$ in the present study and Borisov and Walker (2000) increase with decreasing fO_2. From the slope of $D_{Os}^{met/sil}$ in dependence on $\log fO_2$, both data sets favour predominantly Os^{3+} as main species dissolved inside the silicate melt. Below a threshold of $\log fO_2 = -8.3$, determined $D_{Os}^{met/sil}$ are dominated by the nanonugget problem. This results in a termination of the previously observed trend of $D_{Os}^{met/sil}$ with decreasing fO_2, while lowering the determined $D_{Os}^{met/sil}$ by about one order of magnitude. This is accompanied by an increase of the scatter in the obtained data by roughly one order of magnitude, without showing any further evidence for a dependence on fO_2 whatsoever.

Extrapolation of the obtained data to core relevant fO_2 conditions (Os^{3+}, IW-2; 3000 K: under the assumptions and neglections mentioned above) result in a $D_{Os}^{\text{Fe liq},\infty/\text{sil}} = 1.5 \times 10^5$, and therefore slightly lower than the above mentioned calculations. However, results of all studies remain between 2 and 4 orders of magnitude higher in comparison to values required for core-mantle equilibrium ($D_{Os}^{\text{Fe liq},\infty/\text{sil}} = \sim 10^3$).

Nevertheless, it should be emphasised that temperature, in particular, is potentially a very important variable beside changes in pressure, silicate and sulfide melt composition, which could change the metal/silicate melt partitioning of HSE (e.g., Walter et al., 2000) if very high temperature conditions for magma ocean scenarios are assumed. On the other hand, results from Borisov and Palme (1997) showed that Pt solubility increases only slightly with increasing NBO/T (increasing NBO/T from ~0.5 to ~1.3 leads to an increase in the solubility of Pt

of only ~0.2 log-units), and Ertel et al. (in press) and Holzheid et al. (2000) demonstrated, that pressure has not the decreasing effect on metal/silicate melt partitioning of Pt, as was expected.

Assuming, that Os exhibits a similar behaviour to that of Pt in respect to pressure, temperature and melt compositional effects, the present data and data from previous studies indicate, that high-pressure/high-temperature core-mantle equilibrium during accretion of the Earth cannot explain the absolute elemental depletions in the Earth's mantle. Moreover, in the hypothesis of such an equilibrium core formation, given the relative abundance ratios of the highly siderophile elements in the Earth's mantle of approximately unity, the partition coefficients of those elements extrapolated from solubility studies should all result in similar values. The Fe liquid/silicate melt partition coefficients reported for Pt and Rh in Fortenfant et al. (2002) are 4.4×10^8 for Pt and 1.6×10^6 for Rh, respectively. The partition coefficients of Os, Pt and Rh are then orders of magnitude different, which is not coherent with equilibrium core formation. This observation was already observed and pointed out by studies of Fleet and Stone (1991), Fleet et al. (1991), and Walter et al. (2000).

In summary, the abundances and relative chondritic elemental ratios observed for highly siderophile elements in the Earth's mantle are, though, more likely to be formed by the accretion of a late veneer of chondritic material after core formation had already ceased.

6. Conclusions

Os solubility results obtained in the present study confirm the very highly siderophile character of Os with a solubility of 234 ppb at 10^5 Pa (= 1 bar), 1350 °C and $\log f O_2 = -7$. For an oxygen fugacity higher than 10^{-8} bars, the solubility of Os in melt increases with increasing oxygen fugacity. This behaviour is in perfect agreement with a valence state of 3+ for Os in the melt. For an oxygen fugacity lower than 10^{-8} bars, nanonugget contamination—shown by LA-ICP-MS and SEM analyses—has affected the analysis leading to an overestimation of the solubilities of Os in the melt. Even applying the MAE technique of Dingwell et al. (1994) was not sufficient to circumvent or avoid the nanonugget formation and its problems on concentration determinations entirely. However, the present data at high oxygen fugacities (above $\log f O_2 = -8$) are about 0.7 log units below previous studies, using as well a bulk analytical technique, and extending reliable equilibrium values of Os to even lower concentration levels. Equally critical is the analytical method chosen: for HSE studies, spot analytical techniques like LA-ICP-MS are preferable due to its ability to avoid nanonuggets during concentration determinations. However, attempted analyses failed based on the too high Os background signal (already on ppb-level) of the existing Os standards for LA-ICP-MS. Analytical improvements (either of LA-ICP-MS sensitivity or development of a new microanalytical technique able to analyse sub-ppb concentrations of HSE are now required if accurate solubility data for Os and other HSE) are to be obtained. For more reliable extrapolations of metal/silicate melt partition coefficients of Os to conditions, relevant for core formation, the still unknown effects of variables like temperature, pressure and as well melt composition have to be investigated in future experiments to enable a more thorough discussion about accretion scenarios for Earth and other terrestrial planets.

Acknowledgments

This study was supported by the German Research Foundation (DFG: Gerhard-Hess-Research Prize Di 431/3) grants to D.B. Dingwell. Many thanks go to Detlef Krauße for help with the electron microprobe analyses. Reviews by Herbert Palme and two unknown reviewers helped to improve the quality and clarity of the present paper.

Associate editor: J. Kelly Russell

References

Birck, J.L., RoyBarman, M., Campas, F., 1997. Re–Os isotopic measurements at the femtomole level in natural samples. *Geostandard. NewsLett.* **20**, 19–27.

Borisov, A., Palme, H., Spettel, B., 1994. The solubility of palladium in silicate melts: implications for core formation in the Earth. *Geochim. Cosmochim. Acta* **58**, 705–716.

Borisov, A., Palme, H., 1995. The solubility of iridium in silicate melts: new data from experiments with $Ir_{10}Pt_{90}$ alloys. *Geochim. Cosmochim. Acta* **59**, 481–485.

Borisov, A., Palme, H., 1996. Experimental determination of the solubility of gold in silicate melts. *Miner. Petrol.* **56**, 297–312.

Borisov, A., Palme, H., 1997. Experimental determination of the solubility of platinum in silicate melts. *Geochim. Cosmochim. Acta* **61**, 4349–4357.

Borisov, A., Palme, H., 1998. Experimental determination of osmium metal-silicate partitioning coefficient. *Neues Jb. Miner. Abh.* **172**, 347–356.

Borisov, A., Walker, R.J., 2000. Osmium solubility in silicate melts: new efforts and results. *Am. Mineral.* **85**, 912–917.

Chabot, N.L., Agee, C.B., 2001. The effect of core-mantle differentiation on V, Cr, and Mn: Experimental metal/silicate partitioning results. *LPSC* **XXXII**, abstract #1686, Houston.

Chabot, N.L., Agee, C.B., 2002. The behavior of nickel and cobalt during core formation. *LPSC* **XXXIII**, abstract #1009, Houston.

Dingwell, D.B., Ertel, W., O'Neill, H.St.C., Spettel, B., 1994. The solubility and oxidation state of nickel in silicate melt at low oxygen fugacities: results using the mechanically assisted equilibration technique. *Geochim. Cosmochim. Acta* **58**, 1967–1974.

Ertel, W., 1996. Bestimmung des Löslichkeitsverhaltens und der Metall-Silikat-Verteilungs-koeffizienten der siderophilen Elemente (Ni, W, Ir, Pt, Rh und Re) in einer haplobasal-tischen Schmelze bei hohen Temperaturen. PhD Thesis, 154 pages, BGI, University of Bayreuth.

Ertel, W., O'Neill, H.S.t.C., Dingwell, D.B., Spettel, B., 1996. Solubility of tungsten in a haplobasaltic melt as a function of temperature and oxygen fugacity. *Geochim. Cosmochim. Acta* **60**, 1171–1180.

Ertel, W., Dingwell, D.B., O'Neill, H.St.C., 1997. Compositional dependence of the activity of nickel in silicate melt. *Geochim. Cosmochim. Acta* **61**, 4707–4721.

Ertel, W., O'Neill, H.St.C., Sylvester, P.J., Dingwell, D.B., 1999. Solubility of Pt and Rh in haplobasaltic silicate melts. *Geochim. Cosmochim. Acta* **63**, 2439–2449.

Ertel, W., O'Neill, H.St.C., Sylvester, P.J., Dingwell, D.B., Spettel, B., 2001. The solubility of rhenium in silicate melts: implications for the geochemical properties of rhenium at high temperature. *Geochim. Cosmochim. Acta* **65**, 2161–2170.

Ertel, W., Drake, M.J., Walter, M.J., Sylvester, P.J. (in press for GCA). Experimental study of the solubility and partitioning behaviour of platinum up to 14 GPa and 1950 °C: Implications for Accretion and Core Formation in the Earth.

Fleet, M.E., Stone, W.E., 1991. Partitioning of platinum-group elements in the Fe-Ni-S system and their fractionation in nature. *Geochim. Cosmochim. Acta* **55**, 245–253.

Fleet, M.E., Tronnes, R.G., Stone, W.E., 1991. Partitioning of platinum group elements in the Fe-O-S system to 11 GPa and their fractionation in the mantle and meteorites. *J. Geophys. Res.* **96**, 21949–21958.

Fortenfant, S.S., Günther, D., Dingwell, D.B., Rubie, D.C., 2002. Temperature dependence of Pt and Rh solubilities in a haplobasaltic melt. *Geochim. Cosmochim. Acta* **67**, 123–131.

Gessmann, C.K., Rubie, D.C., 1998. The effect of temperature on the partitioning of nickel, cobalt, manganese, chromium, and vanadium at 9 GPa and constraints on formation of the earth's core. *Geochim. Cosmochim. Acta* **62**, 867–882.

Gessmann, C.K., Rubie, D.C., 2000. The origin of the depletions of V, Cr, and Mn in the mantles of the Earth and Moon. *Earth Planet. Sci. Lett.* **184**, 95–107.

Holzheid, A., Grove, T.L., 2002. Sulfide saturation limits in silicate melts and their implications to core formation scenarios for terrestrial planets. *Am. Mineral.* **87**, 227–237.

Holzheid, A., Borisov, A., Palme, H., 1994. The effect of oxygen fugacity and temperature on solubilities of nickel, cobalt, and molybdenum in silicate melts. *Geochim. CosmoChim. Acta* **58**, 1975–1981.

Holzheid, A., Sylvester, P., O' Neill, H.St.C., Rubie, D.C., Palme, H., 2000. Evidence for a late veneer in the Earth's mantle from high-pressure partitioning of palladium and platinum. *Nature* **406**, 396–399.

Li, J., Agee, C., 1996. Geochemistry of mantle-core formation at high pressure. *Nature* **381**, 686–689.

Li, J., Agee, C.B., 2001. The effect of pressure, temperature, oxygen fugacity and composition on partitioning of nickel and cobalt between liquid Fe-Ni-S alloy and liquid silicate: implications for the Earth's core formation. *Geochim. Cosmochim. Acta* **65** (11), 1821–1832.

O'Neill, H.St.C., 1991a. The origin of the Moon and the early history of the earth– a chemical model. Part 1: the Moon. *Geochim. Cosmochim. Acta* **55**, 1135–1157.

O'Neill, H.St.C., 1991b. The origin of the Moon and the early history of the Earth—a chemical model. Part 2: the Earth. *Geochim. Cosmochim. Acta* **55**, 1159–1172.

O'Neill, H.St.C., Pownceby, M.I., 1993. Thermodynamic data from redox reactions at high temperatures. I. An experimental and theoretical assessment of the electro-chemical method using stabilized zirconia electrolytes with revised values for Fe-"FeO", Co-CoO, Ni-NiO and Cu-Cu_2O oxygen buffers, and new data for the W-WO_2 buffer. *Contrib. Mineral. Petr.* **114**, 296–314.

Okamoto, H., 1992. Ni-Re (nickel-rhenium). *J. Phase Equilib.*, **13**, 335.

Pouchou, J.L., Pichoir, F., 1984. A new model for quantitative x-ray microanalysis—part 1: application to the analysis of homogeneous samples. *Res. Aerospat.* **3**, 13–38.

Righter, K., Drake, M.J., 1997. Metal-silicate equilibrium in a homogeneously accreting earth: new results for Re. *Earth Planet. Sci. Lett.* **146**, 541–553.

Righter, K., Drake, M.J., Yaxley, G., 1997. Prediction of siderophile element metal-silicate partition coefficients to 20 GPa and 2800 °C: the effects of pressure, temperature, oxygen fugacity, and silicate and metallic melt compositions. *Phys. Earth Planet. Inter.* **100**, 115–134.

Swartzendruber, L.J., Sundman, B., 1983. Fe-Os (iron-osmium). *Bull. Alloy Phase Diagrams* **4**, 396–399.

Sylvester, P.J., Eggins, S.M., 1997. Analysis of Re, Au, Pd, Pt, and Rh in NIST glass certified reference materials and natural basalt glasses by laser-ablation ICP-MS. *Geostandard. NewsLett.* **21**, 215–228.

Wänke, H., 1981. Constitution of terrestrial planets. *Philos. Trans. R. Soc. Lond.* **303**, 287–302.

Walter, M.J., Thibault, Y., 1995. Partitioning of tungsten and molybdenum between metallic liquid and silicate melt. *Science* **262**, 1858–1861.

Walter, M.J., Newsom, H.E., Ertel, W., Holzheid, A., 2000. Siderophile elements in the Earth and Moon. Metal/Silicate partitioning and implication for core formation. In: Canup, R.M., Righter, K. (Eds.), *Origin of the Earth and Moon*. University of Arizona Press, Tucson, pp. 265–289.